AGU PUBLICATIONS

Journal of Advances in Modeling Earth Systems

RESEARCH ARTICLE

10.1002/2014MS000370

The influence of misrepresenting the nocturnal boundary layer on idealized daytime convection in large-eddy simulation

Bart J. H. van Stratum[1,2] and Bjorn Stevens[1]

[1]Max Planck Institute for Meteorology, Hamburg, Germany, [2]International Max Planck Research School on Earth System Modelling, Hamburg, Germany

Key Points:
- A resolution study for the diel cycle of dry convection in LES was performed
- Misrepresenting the NBL only has a small influence on daytime convection in LES
- Low-resolution LES can be appropriate to study the diel cycle of convection

Correspondence to:
B. J. H. van Stratum,
bart.vanstratum@mpimet.mpg.de

Citation:
van Stratum, B. J. H., and B. Stevens (2015), The influence of misrepresenting the nocturnal boundary layer on idealized daytime convection in large-eddy simulation, *J. Adv. Model. Earth Syst.*, *07*, doi:10.1002/2014MS000370.

Received 6 AUG 2014
Accepted 2 MAR 2015
Accepted article online 12 MAR 2015

Abstract The influence of poorly resolving mixing processes in the nocturnal boundary layer (NBL) on the development of the convective boundary layer the following day is studied using large-eddy simulation (LES). Guided by measurement data from meteorological sites in Cabauw (Netherlands) and Hamburg (Germany), the typical summertime NBL conditions for Western Europe are characterized, and used to design idealized (absence of moisture and large-scale forcings) numerical experiments of the diel cycle. Using the UCLA-LES code with a traditional Smagorinsky-Lilly subgrid model and a simplified land-surface scheme, a sensitivity study to grid spacing is performed. At horizontal grid spacings ranging from 3.125 m in which we are capable of resolving most turbulence in the cases of interest to grid a spacing of 100 m which is clearly insufficient to resolve the NBL, the ability of LES to represent the NBL and the influence of NBL biases on the subsequent daytime development of the convective boundary layer are examined. Although the low-resolution experiments produce substantial biases in the NBL, the influence on daytime convection is shown to be small, with biases in the afternoon boundary layer depth and temperature of approximately 100 m and 0.5 K, which partially cancel each other in terms of the mixed-layer top relative humidity.

1. Introduction

Moist convection remains one of the major uncertainties in general circulation models (GCMs), causing biases in (amongst others) the frequency, onset, or spatial distribution of precipitation [*Jakob*, 2010]. Although the complexity of subgrid-scale parameterizations has greatly increased, uncertainties related to clouds and precipitation (CP) continue to exist in current state-of-the-art GCMs [*Stevens and Bony*, 2013]. To increase the understanding and to ultimately improve the representation (parameterization) of CP processes, a number of initiatives exploiting high-performance computing have been launched, for example, the Cascade project [*Holloway et al*., 2012] or high-resolution experiments with NICAM (Nonhydrostatic ICosahedral Atmospheric Model) [*Miyamoto et al*., 2013]. Both initiatives use a (horizontal) grid spacing Δ_x of 1–2 km. For dry and shallow convection, these grid spacings approach the size of the largest convective eddies and convection becomes partially (but poorly) resolved [*Honnert et al*., 2011]. With convection being neither fully resolved, nor fully parameterized, modeling in this area is challenging. As such, grid spacings in the range from ∼500 m to ∼3 km are often referred to as the convective grey zone or terra incognita [e.g., *Wyngaard*, 2004; *Zhou et al*., 2014].

Recently, the German ministry for education and research (BMBF) launched an initiative termed *High-Definition Clouds and Precipitation for Advancing Climate Prediction* [HD(CP)^2]. This initiative strives to perform large-eddy simulation (LES) hind casts of diurnal cycles of convection using horizontal grid spacings of $\Delta_x \approx$ 100m on spatial scales as large as Germany (1000^2-1500^2 km), and then expanding the domain size as more computational resources become available with time. In contrast with models relying on the Reynolds-Averaged Navier-Stokes (RANS) equations like standard GCMs, LES at grid spacings of 100 m explicitly resolves the most energetic eddies related to both dry and shallow convection. Thereby, it attempts to leap over the aforementioned modeling issues in the convective grey zone and reduce the uncertainty related to convection. For relatively large domains, these type of experiments can be a useful source of synthetic data to study CP processes in detail.

However, even though grid spacings of 100 m are sufficient to represent convection, it leaves some other processes unresolved. One of these processes, relevant for the diurnal cycle of convection over land, is the

stable nocturnal boundary layer (NBL). Even for weak to moderately stable conditions, LES of the NBL requires a grid spacing of $\mathcal{O}(1\,\mathrm{m})$ [*Beare et al*., 2006], which greatly increases the computational burden. To illustrate this point, consider that every doubling of resolution (at a constant Courant number) increases the computational costs with roughly a factor 16. A grid refinement from current limited-area models (e.g., COSMO-DE at $\Delta_x = 2800$ m) [*Baldauf et al*., 2011] to convection resolving experiments ($\Delta_x = 100$ m) implies a computational increase of $\mathcal{O}(10^5 - 10^6)$, which is ambitious but conceivable in the near future. An additional increase in computational costs of $\mathcal{O}(10^8)$, which would be required for $\Delta_x = 1$ m, is not. If the representation of the NBL ends up being crucial to the development of convective processes during the day this bodes poorly for attempts to use more fundamental approaches, like LES, to understand CP processes. So do we need to resolve the NBL to accurately study daytime convection?

The NBL plays a crucial role in numerical weather prediction (NWP, e.g., near-surface temperatures, fog or air pollution) [*Fernando and Weil*, 2010; *Holtslag et al*., 2013], but these details might be of secondary importance for studies focused on the daytime convective boundary layer (CBL). From this perspective, some errors in the representation of the NBL may be tolerable, as long as they do not significantly influence the development or characteristics of the CBL. *Vilà-Guerau de Arellano* [2007] demonstrated with different methods that differences in the early morning characteristics of the NBL and free troposphere can significantly effect daytime convection and the formation of shallow cumulus. Whether such different initial conditions can arise from a poorly represented NBL in low-resolution LES is currently unknown.

As LES modeling of the diurnal cycle of convection requires both a sufficiently sized domain to capture the large convective eddies, and high resolution to resolve the small-scale nocturnal eddies, the NBL and CBL have primarily been addressed individually [e.g., *Mason and Derbyshire*, 1990; *Brown et al*., 2002]. The implications of underresolving the NBL were—to some extent—addressed in the first Global Energy and Water Cycle Exchanges Project (GEWEX) Atmospheric Boundary Layer Study (GABLS1) LES intercomparison [*Beare et al*., 2006]. Their results indicate that with decreasing resolution the NBL deepens, but their range of grid spacings was limited to $\Delta_x \leq 12.5$ m, and without addressing the development of convection on the subsequent day. Only recently has the increase in computational resources and development of dynamic subgrid-scale (SGS) models made LES studies covering (near) full diurnal cycles possible [*Kleissl et al*., 2006; *Kumar et al*., 2006; *Basu et al*., 2008a; *Kumar et al*., 2010].

Despite their promising results, these dynamic schemes require a sufficiently resolved turbulence field to determine the subgrid-scale parameters. Prior to this study, we tested two more advanced subgrid models for the GABLS1 case: the scale-dependent Lagrangian dynamic model [*Bou-Zeid et al*., 2005; *Huang et al*., 2008] and the stretched-vortex model [*Chung and Matheou*, 2014]. Although both schemes perform well when turbulence is moderately underresolved, they fail at the coarse grid spacings addressed in this study, where turbulent mixing ceases. For this reason, and because we anticipate that simple subgrid-scale closures will remain attractive for convective-scale modeling, the remainder of this study focuses on the traditional Smagorinsky-Lilly model.

What happens if we simulate the diurnal cycle of convection using an LES setup with a crude representation of the SGS processes, with (horizontal) grid spacings as coarse as 100 m? How poorly is the NBL represented, and could potential biases in its development influence daytime convection? We address these questions with a number of idealized experiments covering a near-complete diel cycle of convection over land.

To develop a foundational understanding of these issues, our study focuses on the dynamical aspects: the ratio of explicitly resolved turbulence versus the fraction modeled by the SGS model at various grid spacings, and its implication for the NBL development and the development of the subsequent day of convection for a dry case (no moisture). Although both moisture and radiation are likely to be relevant to many situations [e.g., *Duynkerke*, 1999], the issues that we investigate are likely to be common to all cases. With moist convection being rooted in the dry subcloud layer [e.g., *van Stratum et al*., 2014], any issues with representing such a relatively simple dry CBL are inevitably going to be reflected on the development and characteristics of more complex cases with moist convection. To design the experiments, we first obtain the typical summertime NBL characteristics from measurement data representative for Western European conditions. This region was chosen for focus because of its relevance for HD(CP)^2 and availability of meteorological measurement sites at Cabauw (Netherlands) and Hamburg (Germany). Deriving typical boundary

forcings like wind speed and surface cooling allow for the design of numerical experiments that cover the observed conditions, without having to deal with what we believe to be secondary details (e.g., case specific, complicated synoptic-scale forcings). For each experiment, we perform a sensitivity study on resolution, ranging the grid spacing from 3.125 m in which we are capable of resolving most turbulence in the cases of interest, to grid a spacing of 100 m which is clearly insufficient to resolve the NBL. In attempting to focus on the most basic issues that will be common to almost every type of NBL, we have found it nonetheless necessary to include a minimal land-surface model (LSM) as a lower boundary condition. Early experiments using prescribed surface fluxes, or even a prescribed surface temperature (tendency) proved to prevent the ABL from responding to surface biases, and vice versa. The response introduced by the LSM can potentially enhance biases, but has also proven to decrease the intermodel spread of results [*Holtslag et al*., 2007]. Furthermore, the use of prescribed fluxes can lead to inconsistencies in the surface layer parameterization in the NBL [*Basu et al*., 2008b].

The remainder of this paper is organized as follows: section 2 presents an analysis of the measurement data. In section 3, the LES code is briefly introduced, together with a description of the case setup. Our main findings are presented in section 4, first in terms of the general characteristics of the experiments, followed by the results of the sensitivity study on resolution. Finally, the results are summarized in section 5.

2. Characteristics of the Clear Summertime Nocturnal Boundary Layer

To setup the numerical experiments, we first obtain relevant NBL characteristics from measurements. This allows us to design a number of experiments that cover the characteristics of the desired study area. The analysis is based on 12 years of data (1 January 2001 to 12 December 2012) from two meteorological sites in Western Europe: the Hamburg weather mast operated by the University of Hamburg, Germany, and the Cabauw Experimental Site for Atmospheric Research (CESAR) in Cabauw, Netherlands. The Hamburg site is located in the easterly outskirts of Hamburg (53.52°N, 10.10°E) and characterized by flat but inhomogeneous surroundings comprising a mix of industrial buildings and community gardens, with rural terrain toward the east [*Brümmer et al*., 2012]. The Cabauw site (51.97°N, 4.93°E) is surrounded by flat terrain and open pasture in all directions, with some low buildings at 400–600 m distance toward the north and east [*Van Ulden and Wieringa*, 1996].

Because of the present study's focus on daytime convection, we limit the analysis to clear nights during the May to August period (see Appendix A for details and a validation of the sampling procedure). We focus the analysis on two key features that govern the characteristics of the NBL: wind (shear production of turbulence) and surface cooling (buoyancy suppression as the atmosphere becomes stably stratified). Wind speeds are obtained from tower measurements at 200 m height (direct measurement for Cabauw, interpolated between 175 and 250 m for Hamburg), and will be used as a proxy for the geostrophic wind. For surface cooling, two measures are used: the surface (skin) temperature obtained from IR-radiometers, and near-surface turbulent heat fluxes obtained from sonic anemometers (5 m height at Cabauw, 10 m height at Hamburg). For all variables, we examine the time development since sunset. Although the NBL development (negative surface flux) usually begins before sunset, this provides a simple robust and objective way to temporally align the data.

The statistics from both stations show typical characteristics of the NBL, with a strong decrease in surface temperature and negative surface fluxes. The results are summarized in Figure 1. For each variable, its time development is summarized by means of 2-D histograms, with the probability binned over 1 h intervals since sunset ($t = 0$ h), and each individual hourly bin normalized to unity. For surface cooling, the temperature at sunset is subtracted from the samples to obtain the net cooling over the night. In all plots, the dashed and solid lines indicate the 25th (P1), 50th (P2), and 75th (P3) percentiles. The 200 m wind speed (Figures 1a and 1d) is relatively similar for both stations—average wind speeds are $\sim$7.5 m s^{-1}, where $\sim$75% of the samples have a wind speed higher than 5 m s^{-1}. Both stations experience a light increase in wind speed during the night, which most likely represents the formation of a low-level jet, and is most evident at Cabauw. In contrast with the relatively similar wind speeds, the surface cooling rate (Figures 1b and 1e) and sensible heat flux (Figures 1c and 1f) differ more between the two stations. The total surface cooling at 9 h after sunset is approximately 9 K in Hamburg, which is 5 K more than in Cabauw, while the sensible heat flux in Cabauw is significantly more negative. A possible explanation for these differences might lie in the difference in near-surface wind speed (not shown), which is lower in Hamburg, likely due to its more sheltered location. However, these interpretations should be tempered by the realization that the fluxes are

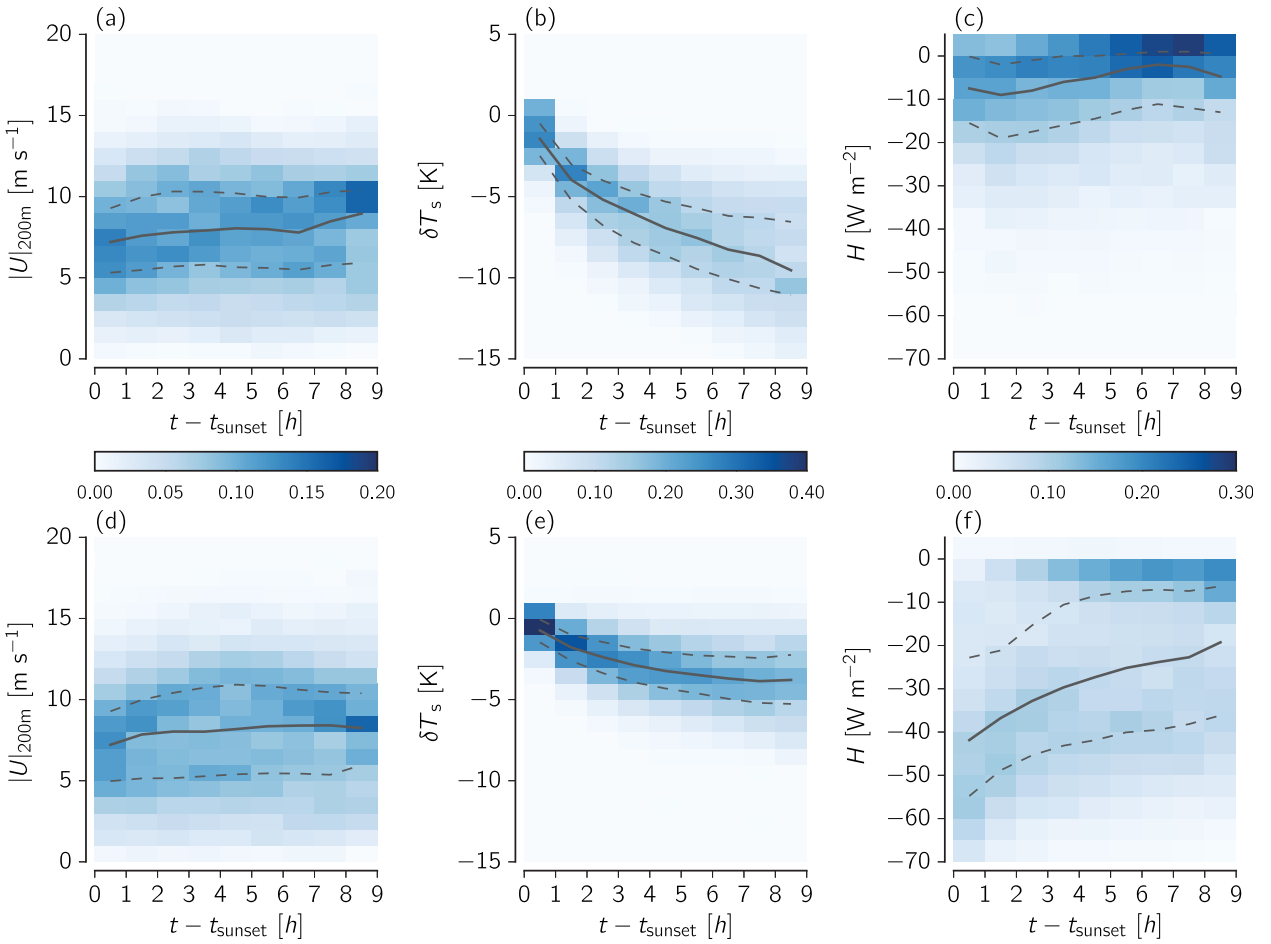

Figure 1. Two-dimensional histograms ((a–c) Hamburg and (d–f) Cabauw) for (left) the absolute wind speed at 200 m height ($|U|_{200m}$), (middle) change in surface temperature since sunset (δT_s), and (right) surface sensible heat flux (H). For each variable, both stations share the color bar. All samples are binned in hourly intervals, and the resulting histograms are normalized per bin (i.e., the total probability per hourly bin equals 1). The dashed lines indicate the 25th and 75th percentile and the solid line the median.

measured at different heights (decreasing heat flux with height), and that there are known difficulties in flux measurements in the NBL (surface energy balance closure) [e.g., *de Roode et al.*, 2010].

Based on these findings, the numerical experiments will aim at covering the typical conditions (P1–P3 as a guideline) with wind speeds in the range of 5–10 m s^{-1} and surface heat fluxes of approximately −30 to −40 W m^{-2}. Further details of the experimental set p are provided in section 3.2.

3. Setup

3.1. Large-Eddy Simulation Code

The University of California, Los Angeles large-eddy simulation (UCLA-LES v4.0) code was used for the numerical experiments described in this study [e.g., *Stevens et al.*, 2005]. Briefly summarized, UCLA-LES numerically integrates the filtered Navier-Stokes equations within the anelastic approximation of *Ogura and Phillips* [1962] with (in the absence of moisture) the three wind components and potential temperature (θ) as prognostic variables. Time integration is performed with a third-order Runge-Kutta scheme. Subgrid diffusion is modeled with the Smagorinsky-Lilly model [*Smagorinsky*, 1963; *Lilly*, 1966], with the eddy-viscosity calculated as [e.g., *Pope*, 2000]:

$$\nu = \lambda^2 \tilde{\mathcal{S}} \sqrt{1 - \frac{\mathrm{Ri}}{\mathrm{Pr_t}}}, \tag{1}$$

with λ the mixing length scale, $\tilde{\mathcal{S}}$ the filtered rate of strain, Ri the Richardson number, and $\mathrm{Pr_t}$ the (prescribed as 1/3) turbulent Prandtl number. The stability correction follows *Lilly* [1962]. $\tilde{\mathcal{S}}$ is defined as:

$$\tilde{\mathcal{S}}=(2\tilde{s}_{ij}\tilde{s}_{ij})^{1/2},\ \tilde{s}_{ij}=\frac{1}{2}\left(\frac{\partial\tilde{u}_i}{\partial x_j}+\frac{\partial\tilde{u}_j}{\partial x_i}\right). \tag{2}$$

The (uncorrected) mixing length scale is defined as $\lambda_0=(C_s\Delta)$, with C_s the Smagorinsky constant and $\Delta=(\Delta_x\Delta_y\Delta_z)^{1/3}$ the grid spacing. Near the surface, the mixing length scale is reduced [*Mason and Thomson*, 1992]:

$$\frac{1}{\lambda^2}=\frac{1}{\lambda_0^2}+\frac{1}{(\kappa z)^2}, \tag{3}$$

with κ the von Kármán constant (0.4) and z the height above the surface. Based on a validation (not shown) for the GABLS1 LES intercomparison [*Beare et al*., 2006], a few minor adjustments were made: the addition of a fourth-order centered advection scheme for scalars [*Wicker and Skamarock*, 2002], and the Smagorinsky constant (C_s) was reduced from 0.23, its default value in UCLA-LES, to 0.17. In addition to these adjustments, we added a minimal land-surface model (LSM) that allows for a response of the surface temperature and turbulent fluxes to biases in the atmosphere, and vice versa. The LSM is based on the *ECMWF* [2011] documentation, and described in Appendix B. Although radiative cooling of the NBL can be significant (especially near the surface and NBL top), its influence on the mean thermodynamic structure is typically small [*Garratt and Brost*, 1981]. Therefore, we follow previous work on idealized NBL experiments [e.g., *Beare et al*., 2006; *Basu et al*., 2008a; *Kosovic and Curry*, 2000], exclude the influence of radiation on the atmosphere, and use a simplified representation for radiation which only drives the LSM. The incoming longwave radiation is set constant in time, and its outgoing component is based on the surface temperature and Stefan-Boltzmann's law. The incoming shortwave radiation is prescribed, using a fixed surface albedo to calculate the outgoing radiation. See Appendix B for details.

3.2. Case Description

The findings of section 2 informed the design of the numerical experiments, which we here describe. All cases cover a near-complete diel cycle (21 h), running from the late afternoon, throughout the night, into the second day with dry convection. The model is initiated with a 500 m deep well-mixed layer of potential temperature $\theta = 290$ K, with a constant temperature stratification of 6 K km^{-1} above. The diurnal variability is introduced by the parameterized radiation and LSM (Appendix B). In the late afternoon (start of the experiment), solar heating drives convection and growth of the CBL. When the net surface radiation (Q_{net}) becomes negative, surface cooling and the development of the NBL are initiated. In time, the NBL deepens as the cool surface air is mixed upward by turbulent eddies, whose intensity is partially regulated by wind shear. Based on the findings of section 2, we initially consider two experiments in which only the geostrophic wind is varied from 5 to 10 m s^{-1} (Table 1). As shown in section 2, the lower threshold of 5 m s^{-1} ensures that we cover approximately 75% of the typical Western European conditions. In addition to wind shear, the surface cooling rate determines the turbulent intensity as it drives the formation of the stable layer, which suppresses (vertical) turbulent motions. Although the inclusion of the LSM obstructs us from directly controlling the surface cooling, we can manipulate the cooling rate through the surface characteristics in the following way: by decreasing the thermal conductivity of the skin layer (Λ_{sk}, equation (B3)), the interaction between the surface and soil is decreased, increasing the atmospheric cooling rate at night (experiment U_{8L}). After sunrise, the surface is heated again, a shallow CBL forms in the stable layer, until convection grows into the residual layer of the previous day of convection. Note that in the absence of large-scale forcings (advection, subsidence) and radiation, there is no process stabilizing the residual layer after the onset of the NBL.

Table 1. Overview of the Three Different (Physical) LES Experiments, Varying the Geostrophic Wind (U_g) and conductivity of the Skin Layer (Λ_{sk}, Equation (B3))[a]

Exp	U_g (m s^{-1})	Λ_{sk} (W m^{-1} K^{-1})
U_{10}	10	10
U_5	5	10
U_{8L}	8	1

[a]The domain is oriented such that the geostrophic wind is in the x direction, and the v component is set to zero.

Combined, the variation in geostrophic wind and surface cooling rate results in three physical experiments, summarized in Table 1. For each physical experiment, sensitivity studies on resolution are performed. All cases fix the domain size to $L_x=L_y=3200$ m, $L_z=2000$ m, in which the grid spacing is varied from $\Delta_{xy}=\Delta_z=3.125$ m to $\Delta_{xy}=100$ m, $\Delta_z=25$ m (Table 2). Throughout the text, the combination of physical experiment—resolution experiment is referred to as, e.g., $U_{10}-\Delta_3$ for the 10 m s^{-1} case with a grid spacing of 3.125 m. Except for the

Table 2. Resolution Experiment[a]

Exp	N_{xy} (–)	N_z (–)	Δ_{xy} (m)	Δ_z (m)	C_s
Δ_3 (reference)	1024	640	3.125	3.125	0.17
Δ_3−Cs	1024	640	3.125	3.125	0.10
Δ_6	512	320	6.25	6.25	0.17
Δ_{12}	256	160	12.5	12.5	0.17
Δ_{25}	128	80	25	25	0.17
Δ_{50}	64	80	50	25	0.17
Δ_{100}	32	80	100	25	0.17

[a]All experiments fix the horizontal domain size to 3200 m and the vertical size to 2000 m.

variation in grid spacing, the resolution experiments share the exact same setup—no tuning of (for example) parameters in the SGS model is performed. However, to verify the validity of the U_5 and U_{8L} experiments, two additional runs were performed for a part of the NBL period with a decreased Smagorinsky constant (case name appended with Cs). All horizontal velocities are initiated with their geostrophic value, constant with height. Temperature perturbations are applied to the initial mixed layer to break the horizontal slab symmetry. Although sufficiently turbulent LES is stochastic [e.g., *Sullivan and Patton*, 2011], the averaging time and domain size provide sufficient sampling so that the statistics are robust, and not influenced by differences among realizations. At the top of the domain, a 200 m deep damping layer (with a time scale linearly increasing from $\tau = 0$ s at 1800 m to $\tau = 300$ s at 2000 m) is added to prevent the reflection of gravity waves. The surface pressure is set to 10^5 Pa, and the base state potential temperature to 296 K.

4. Results

4.1. General Characteristics of the Experiments

We first present the general characteristics of the different experiments from the three high-resolution reference cases ($U_{10}-\Delta_3$, $U_5-\Delta_3$, $U_{8L}-\Delta_3$, Table 2). In addition, the validity of the reference cases will be addressed. Figures 2 and 3 show the temporal evolution of four key atmospheric and surface properties: the ABL depth (z_{ABL}) in Figure 2, and the 10 and 200 m wind speed ($|U|$), surface sensible heat flux (H), and the surface temperature (T_s) in Figure 3. The 200 m wind speed, surface temperature, and surface heat flux in Figure 3 allow for a comparison with the measurement data presented in Figure 1. Note that we do not attempt to validate the model in detail, which would require specific measurements that we do not have access to, but rather compare the experiments with measurement statistics to ensure that our idealized study addresses a relevant part of the parameter space. Two different definitions of the ABL depth are used. For convective conditions ($H > 0$), the ABL depth is defined as the height of the minimum turbulent heat flux. For stable conditions ($H < 0$), the ABL depth is defined as the first height at which the ABL temperature is within 0.25 K of the last temperature profile when H was last larger than zero. In other words, this is the layer depth which is influenced by surface cooling. The definition for stable conditions differs from typical definitions based on the momentum flux or a critical Richardson number [e.g., *Beare et al.*, 2006; *Richardson et al.*, 2013], as both methods have proven to be imprecise for our experiments because of decaying turbulence in the residual layer.

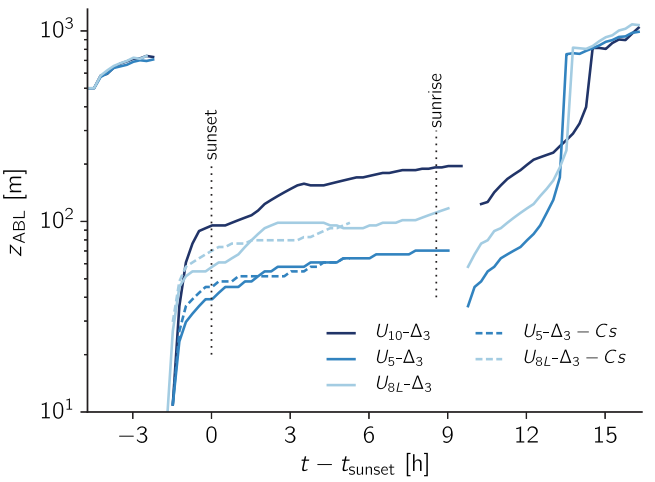

Figure 2. Temporal evolution of the ABL depth (z_{ABL}) in the three reference cases (U_{10}-Δ_3, U_5-Δ_3, U_{8L}-Δ_3) and the two sensitivity experiments on the Smagorinsky constant (U_5-Δ_3-Cs, U_{8L}-Δ_3-Cs). As explained in the text, different ABL-depth definitions for convective and stable conditions are used, resulting in two discontinuities before and after sunset.

Although the surface temperature (Figure 3b) decreases over the first few hours before sunset, the surface sensible heat flux (Figure 3c) remains positive resulting in convection and growth of the mixed layer up to approximately 800 m height. From case $U_5-\Delta_3$ to $U_{10}-\Delta_3$, the mixed layer slightly deepens because of small differences in H and potentially by shear-driven growth of the mixed layer [*Pino et al.*, 2003]. Approximately 1 h before sunset, T_s begins to decrease rapidly and Q_{net} becomes negative, marking the onset of the NBL. A shallow internal boundary

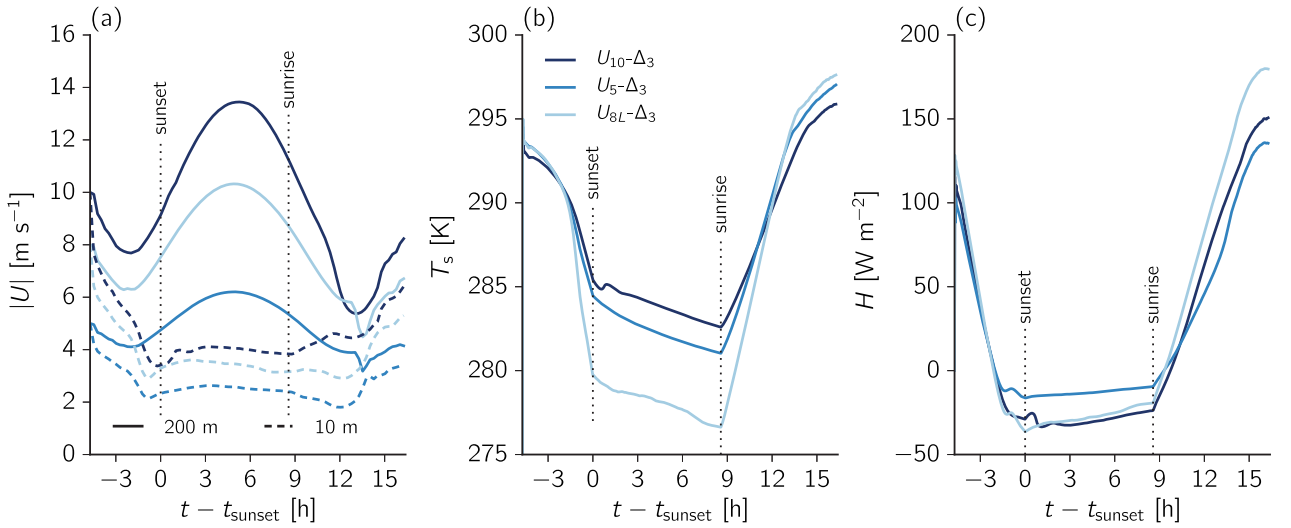

Figure 3. Temporal evolution of the (a) absolute wind speed $|U|=\sqrt{u^2+v^2}$ at 10 and 200 m height, (b) surface sensible heat flux H, and (c) surface (skin) temperature T_s in the U_{10}-Δ_3, U_5-Δ_3, U_{8L}-Δ_3 experiments.

layer develops as the thermally driven mixing shuts down, and the NBL deepens in time as cool air from the surface is mixed upward, where the mixing depth is determined by the intensity of the turbulent eddies. The NBL in the U_{10} case grows to approximately 200 m depth at sunrise. For weaker winds, or less conductive surfaces with stronger surface cooling, the NBL is about half as deep. As observed in the measurement data (Figures 1a and 1d), the wind speed aloft increases over the NBL period and becomes super-geostrophic (low-level jet). Nighttime 200 m wind speeds are in between 4 and 14 m s^{-1}, in line with the analysis for Cabauw/Hamburg. After the rapid decrease in surface temperature shortly before sunset, the cooling rates moderate and remain approximately constant during the night. All cases have their total surface cooling in between 2.9 and 3.4 K, less than observed in the measurement data. However, the resulting surface sensible heat flux (H) is in between -10 and -40 W m^{-2}, which agrees, in both magnitude and tendency, with the findings in Figures 1c and 1f. Despite the simplicity with which the land-surface processes are represented and the idealizations in the setup, the LES cases cover the typical conditions presented in Figure 1, with realistic features in both the CBL and NBL.

To address the validity of the reference (Δ_3) cases during the NBL period, we show in Figure 4 the fraction resolved/total heat flux as a function of the normalized ABL depth (at $t = 10$ h or $t - t_{sunset} \approx 5.5$ h). With a 3 m grid spacing, about 75% of the turbulent heat flux is resolved in the U_{10} case. This ensures that the NBL development is primarily driven by resolved turbulence, and that the contribution of the SGS model is limited. Despite the high resolution, this requirement is more difficult to fulfill for the U_5 and U_{8L} cases which resolve approximately 20% and 40%, respectively. More care must be applied in adopting the Δ_3 as a reference case in this situation. However, based on the U_{10} sensitivities it is possible to sensibly interpret the effect of suboptimal resolutions in these cases, even when the reference case is not fully resolved. However, to test such interferences, Figure 4 shows two additional experiments (case name appended with Cs) for the NBL period in which the Smagorinsky constant was reduced from $C_s = 0.17$ to 0.10. This produces a better resolved turbulent field, less influenced by uncertainties related to the SGS closure.

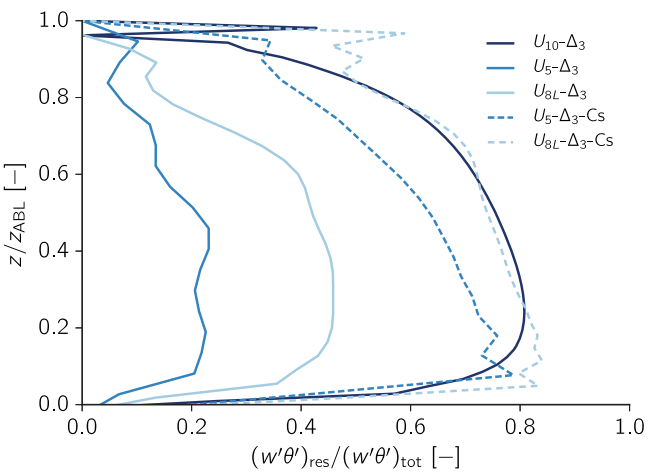

Figure 4. Fraction of resolved/total heat flux in the NBL (t = 10 h) for all Δ_3 cases. For the 5 and 8 m s^{-1} cases, the sensitivity on the Smagorinsky constant (C_s) is shown.

Compared to their counterparts with the reduced Smagorinsky constant, the average NBL depth of the U_5 and U_{8L} cases is off by less than 7% (Figure 2), which indicates that the poor resolution of the reference case is not unduly influencing our experimental setup.

4.2. Case U_{10}: Sensitivity on Resolution

To study the influence of resolution in this section, we present the results from a sequence of simulations in which the resolution is degraded systematically. The resolution is coarsened by factors of two from $\Delta_{xy}=\Delta_z=3.125$ m to $\Delta_{xy}=100$ m, $\Delta_z=25$ m (Table 2) to study (a) how well the NBL is represented at relatively coarse resolutions, and (b) whether biases in the NBL influence the development of convection on the second day. We start with a more detailed analysis of the U_{10} case as it most clearly illustrates the temporal evolution of the cases and their dependence on resolution. Next, the other cases are addressed by studying the ABL biases for both CBL periods and the NBL in section 4.3.

Our analysis focuses on the vertical profiles of potential temperature (θ) and zonal wind (u) at three distinct periods: 2 h before sunset as the surface sensible heat flux becomes negative, sunrise as the NBL has fully developed, and end of the experiment (noon). The results are shown in Figure 5. The markers in the top plots indicate the ABL structure from a bulk perspective, i.e., the height of the ABL (z_{ABL}), and average temperature over that layer ($\langle\theta\rangle$).

4.2.1. Late Afternoon Decay

Over the first hours of convection (Figures 5a and 5d), the results are relatively insensitive to the large difference in grid spacing. Maximum biases in z_{ABL} and $\langle\theta\rangle$ are less than 0.1 K and 30 m, respectively, in line with the findings (first-order moments) of *Sullivan and Patton* [2011]. The velocity profiles are more sensitive, with a small underestimation of the lower-ABL velocity in the low-resolution experiments. This is caused by a small overestimation of the surface friction velocity, and/or the reduced amount of resolved turbulence,

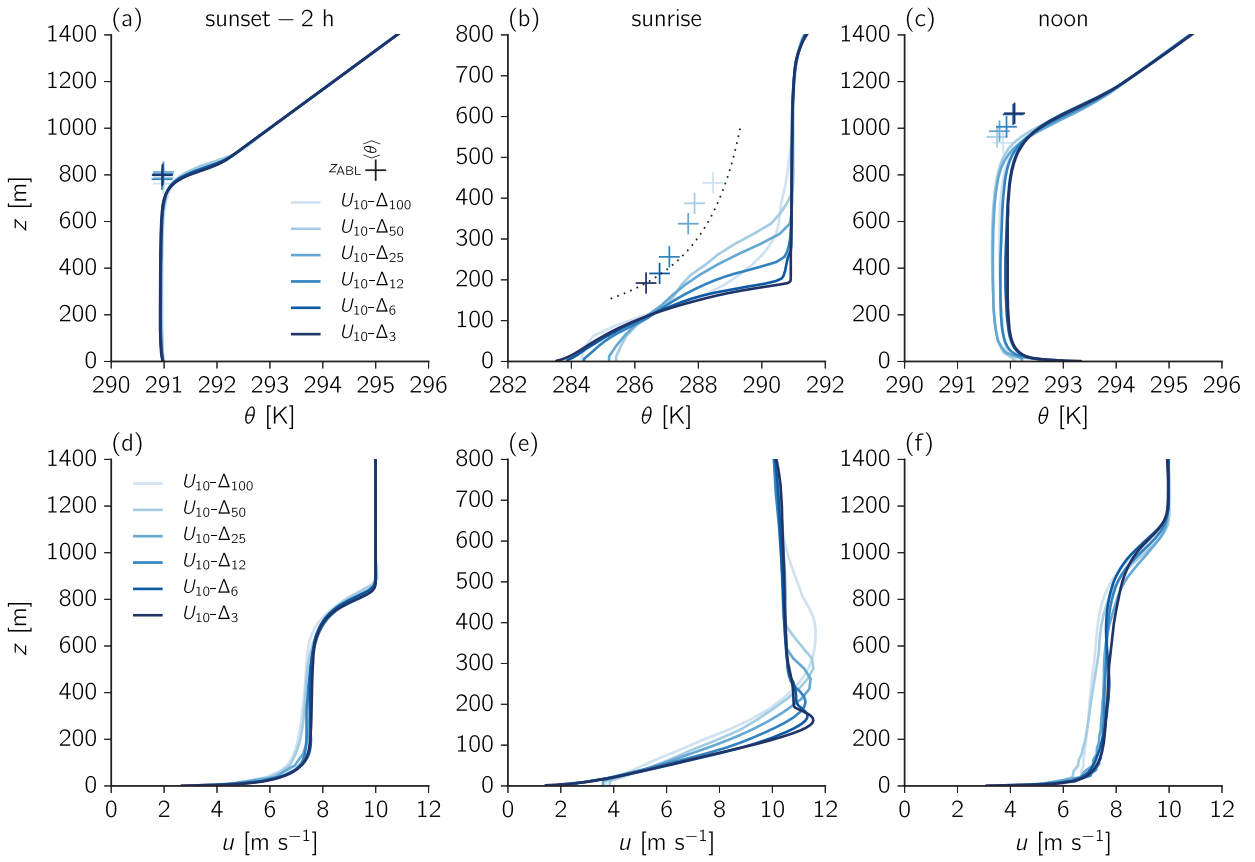

Figure 5. Vertical profiles at sunset minus 2 h (2.75 h), sunrise (13.25 h), and noon (21 h) for case U_{10}. (top) Potential temperature (θ) and (bottom) zonal wind component (u). The markers in the top plots indicate the ABL from a bulk perspective, i.e., the height of the ABL (z_{ABL}), and average temperature over that layer ($\langle\theta\rangle$).

causing more difficulties in maintaining the well-mixed profile. Nonetheless, the resulting biases are small, which are beneficial for our study as it shows that the CBL development itself is insensitive to the range of grid spacings, allowing all cases to enter the NBL phase with similar conditions.

4.2.2. NBL Period

During the NBL period (Figures 5b and 5e), the mean profiles show a greater sensitivity to grid spacing as the more poorly resolved simulations mix through a deeper layer. With increasing grid spacing less turbulence is resolved (percentage resolved/total flux), decreasing from ∼70%–80% in case Δ_3 to ∼10% in case Δ_{25} ($t = 10$ h or $t - t_{\text{sunset}} \approx 5.5$ h, at $z = 0.5\, z_{\text{ABL}}$), the yet coarser resolution experiments (Δ_{50}, Δ_{100}) are nearly laminar. Even though this produces invalid LES (no turbulent mixing; "no-eddy simulation"), there is still diffusive transport by the SGS model. The strain rate—predominantly determined by the vertical shear component of $\tilde{s}_{ij}$ (equation (2))—is fairly constant (Figure 5e). Therefore, with similar strain rate and increasing grid spacing, subgrid diffusion increases which causes the deepening of the NBL. Amongst other possibilities, the use of a shear-improved Smagorinsky scheme [*Lévêque et al.*, 2007] or a more appropriate choice of the subgrid length scale $C_s\Delta$, might improve this undesirable behavior of the SGS model and help it transition to a more standard RANS closure in the absence of a resolved turbulent flow.

The difference in NBL structure is not only caused by the dynamics and/or the SGS model, as in such a case (identical surface heat fluxes) the biases would solely consist of a different redistribution of the cooled air with height. Indicated within Figure 5b (dotted line) is the theoretical NBL structure (bulk temperature/height) that would arise if the total NBL cooling of the Δ_3 case was simply distributed over a different NBL depth. For example, compared to the residual layer temperature of 291 K, the Δ_3-case has cooled 5 K ($\langle\theta\rangle \approx 286$ K) over a 200 m deep layer. Mixing the same cooling over a layer of 400 m depth would theoretically result in 2.5 K NBL cooling, or $\langle\theta\rangle \approx 288.5$ K. Compared to the reference case, all lower-resolution experiments are relatively cold (i.e., situated left of the dotted line), which is the result of the interactive LSM. Shown in Figure 6 is the bias in the surface sensible heat flux compared to the reference case ($\delta H = H_x - H_{\Delta 3}$, with H_x the different U_{10} cases). Approximately 1 h before sunset, the lower-resolution cases start producing more negative surface fluxes. This is the result of an increased temperature difference between the surface and lowest model level, which is partially compensated by an increase in aerodynamic resistance (equation (B2)).

4.2.3. Second Day of Convection

Despite the large biases that are introduced during the NBL period, the different resolution experiments tend to realign during the second day of convection (Figures 5c and 5f). As a result of the additional surface cooling at night (Figure 6), the ABL depth and temperature at the end of the experiments (noon) are lower for the lower-resolution cases, with maximum biases in the mixed-layer depth of ∼100 m, and averaged mixed-layer temperature of ∼0.35 K. Note that the temperature bias is amplified by the difference in mixed-layer growth, influencing the entrainment of relatively warm free tropospheric air as the mixed-layer deepens. The LSM partially compensates these biases as the surface sensible heat flux increases with decreasing resolution (Figure 6). A back of the envelope calculation helps to put these results in perspective: for example, the nighttime bias δH for case Δ_{50} is around -12 W m^{-1} over a period of approximately 12 h (Figure 6). With δH integrated in time, and distributed over the average afternoon mixed-layer depth of 1000 m, this results in a temperature bias of -0.44 K. A similar calculation for the daytime bias ($\delta H \approx 7$ Wm^{-2} over approximately 5 h) reveals a temperature compensation of 0.1 K, indicating that about 25% of the nighttime bias is

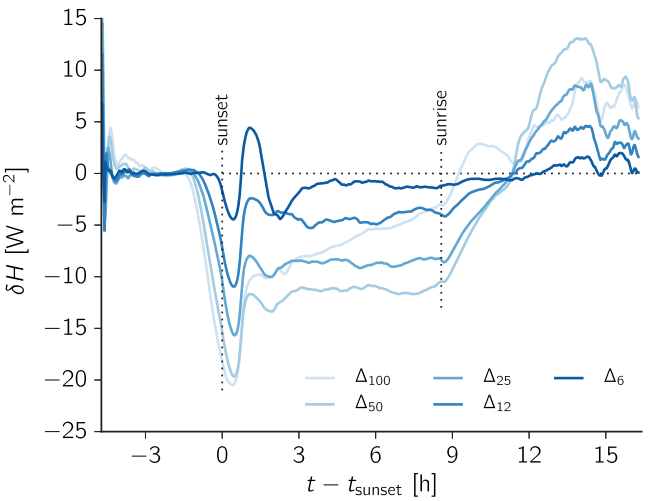

Figure 6. Bias in the surface sensible heat flux for case U_{10}, compared to the U_{10}-Δ_3 case ($\delta H = H_{\Delta_x} - H_{\Delta_3}$).

compensated. As the difference in H remains positive for the low-resolution cases at the end of the experiment, the biases in ABL depth and temperature would further decrease if the experiments were further integrated in time. The partial bias cancellation is not serendipitous, but the result of energy conservation within our experiments where the additional heat entering the soil at night is again released during the day. In section 4.4, the implication of these biases on convection is discussed in more detail.

Summarized, the experiments are insensitive to the large range of grid spacings during the first day of convection. During the NBL phase, the structure of the NBL is influenced by both the ratio of resolved/modeled mixing, and differences in the surface sensible heat flux as the LSM responds to ABL biases, and vice versa. Despite the large NBL biases, all cases tend to realign during the second day of convection.

4.3. Statistics of the U_5, U_{8L}, and U_{10} Cases

For all cases, the biases in ABL depth (δz_{ABL}) and ABL-averaged potential temperature ($\delta\langle\theta\rangle$) are here presented in condensed form (Figure 7). We focus on the same three periods as in the previous section: (i) 2 h before sunset, (ii) sunrise, and (iii) noon during the second day of convection. The biases are calculated compared to the reference (Δ_3) experiments, and all statistics are averaged over the 60 min period before the indicated time.

The results are shown in Figure 7. All three physical experiments exhibit similar behavior. Two hours before sunset ($t = i$) the ABL depth is (on average) slightly underestimated in the lower-resolution experiments, although there is no clear trend as a function of resolution. For all cases, the absolute biases in bulk potential temperature are $\ll$ 0.1 K. During the NBL period the lower-resolution experiments create deeper NBLs. The maximum bias at sunrise ($t = ii$) in z_{ABL} increases with higher wind speeds from ~80 m in the U_5 case to ~250 m for case U_{10}. The relative biases are, however, approximately constant, with the Δ_{100} cases overestimating the NBL depth by 100%–120% compared to the Δ_3 setup. The bulk potential temperature is overestimated in all sensitivity experiments. Although the lower-resolution experiments experience more negative surface heat fluxes (Figure 6 for case U_{10}), the NBL-averaged temperature decreases less as the surface cooling is distributed over a deeper layer. The absolute biases at sunrise ($t = ii$) range from 2 K in case U_{10} to 3 K in case U_{8L}. At noon during the second day of convection ($t = iii$), the biases in ABL depth are opposite in sign of the biases during the NBL period. The U_{8L} and U_{10} cases have the largest underestimation of approximately 100 m. The relatively large bias in $\langle\theta\rangle$ decreases as the mixed layer grows to less than 0.5 K.

Summarized, the misrepresentation of the NBL results in biases in ABL depth and temperature on the order of 100 m and 0.5 K. In the following section, the implications of such biases on cloud formation will be briefly discussed.

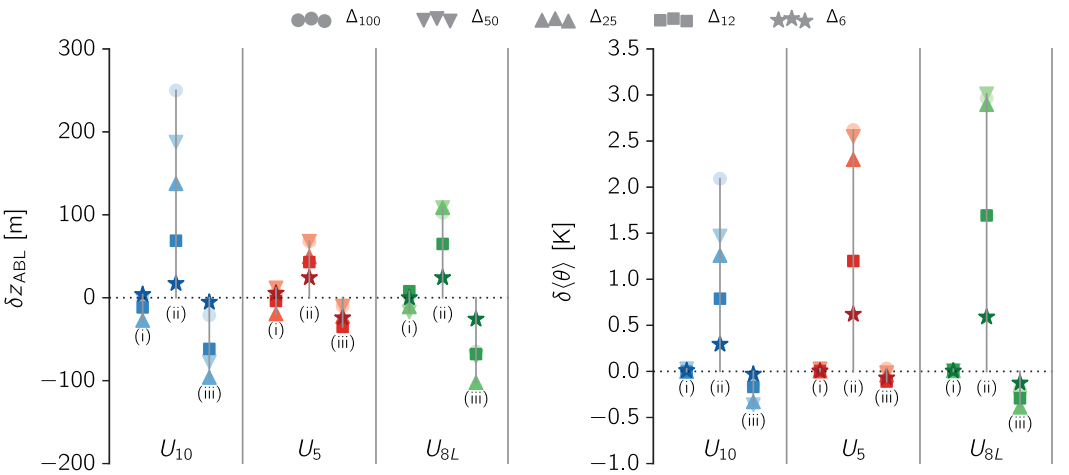

Figure 7. Biases in ABL depth (δz_{ABL}) and ABL-averaged temperature ($\delta\langle\theta\rangle$) at sunset minus 2 h (i, 2.75 h), sunrise (ii, 13.25 h), and noon (iii, 21 h). All statistics are averaged over 1 h (t = 1.75–2.75 h, t = 12.25–13.25 h, and t = 20–21 h).

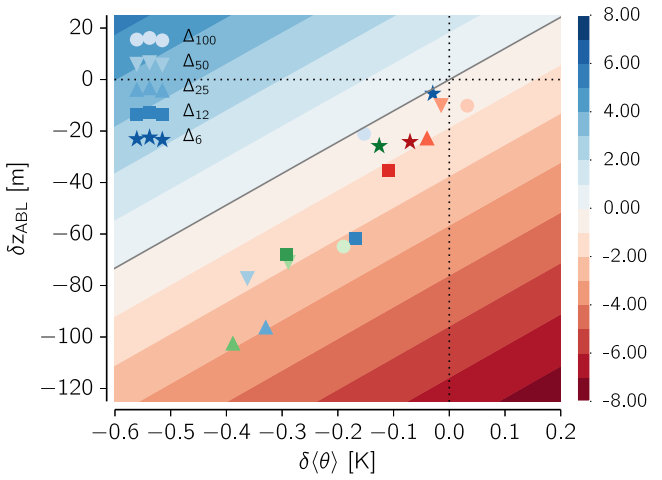

Figure 8. Influence of biases in ABL depth (δz_{ABL}) and temperature $\delta\langle\theta\rangle$ on the mixed-layer top relative humidity (%). Given a bias in z_{ABL} and $\langle\theta\rangle$, the shaded contours indicate the difference in $RH_{z_{ABL}}$ compared to a 1000 m deep ABL with $\langle\theta\rangle = 290$ K and $RH_{z_{ABL}} = 100\%$. The colors of the individual experiments are the same as in Figure 7.

4.4. Implications for Cloud Formation

Up to this point, the biases during the second day of convection have been addressed individually for the ABL depth and temperature. More relevant for moist convection is their contribution to a quantity related to clouds: the mixed-layer top relative humidity ($RH_{z_{ABL}}$). Even though our experiments exclude moisture, we can quantify the temperature contribution to relative humidity biases. These arise both from the effect of mixed-layer temperature biases directly, but also because of an over or underestimation of the mixed-layer depth, influencing the absolute temperature at the mixed-layer top. This thus excludes the influence of ABL dynamics (and biases) on moisture, and only acts to place the biases in mixed-layer temperature and depth in context of $RH_{z_{ABL}}$. Figure 8 shows the results of this analysis. The error in $RH_{z_{ABL}}$ (shaded contours) is here calculated as the combined influence of δz_{ABL} and $\delta\langle\theta\rangle$ on $RH_{z_{ABL}}$, compared to the reference cases (Δ_3). For the reference case, a reference moisture mixing ratio (r_{ref}) is calculated, such that $RH_{z_{ABL}}$ is equal to 100%, i.e., z_{ABL} equals the lifting condensation level. Assuming that r_{ref} is constant amongst the lower-resolution experiments, the bias in mixed-layer potential temperature (directly influencing $T_{z_{ABL}}$) and depth (influencing $T_{z_{ABL}}$ through its dependence on the mixed-layer top pressure) is translated to a bias in $RH_{z_{ABL}}$.

For all cases except one, the biases in z_{ABL} and $\delta\langle\theta\rangle$ are of similar sign: an underestimation of z_{ABL} is coupled to an underestimation of $\langle\theta\rangle$. As the reference cases ($\delta z_{ABL} = \delta\langle\theta\rangle = 0$) are assumed to have a mixed-layer top relative humidity of 100%, their mixed-layer depth corresponds to the height of the lifting condensation level (z_{LCL}). Therefore, for a constant relative humidity, δz_{ABL} corresponds to the change in z_{LCL} as a function of $\delta\langle\theta\rangle$. This allows the comparison of both the change in $RH_{z_{ABL}}$ and $z_{LCL} - z_{ABL}$ from Figure 8.

As shown, the biases in mixed-layer depth and temperature partially compensate. The maximum temperature biases of −0.4 K would result in an increase in relative humidity of 2–3% or change in z_{LCL} of −50 m, which is compensated by the negative bias in mixed-layer depth. The resulting change in $RH_{z_{ABL}}$ is in the range of 0% to −3%, and the difference $z_{LCL} - z_{ABL}$ is on the order of 0 to −50 m. For comparison, these differences are on the order of the intermodel spread (cloud base relative humidity, and cloud base height) of different LES codes for experiments of the daytime ABL only (ARM LES intercomparison) [*Brown et al.*, 2002].

5. Summary and Conclusions

In the present study, we analyzed the influence of misrepresenting the NBL in low-resolution LES on the subsequent day of dry convection. Here low resolution was defined as a grid spacing sufficient to explicitly represent daytime convection, but much coarser than needed to resolve small-scale turbulence in the NBL. With the high requirements on grid spacing for the NBL period, such a setup might be necessary or beneficial for studies that primarily address daytime convection, or early initiatives to explore the use of LES for NWP purposes. We answered the question: how accurately must the NBL be represented in order to obtain a faithful representation of daytime convection?

Using statistics obtained from measurement data representative for summertime Western European conditions, we designed idealized LES experiments covering near-complete diel cycles of convection over land. Reproducing the typically observed conditions ensured that we covered realistic conditions in terms of wind (shear, producing turbulence) and surface cooling (buoyancy suppression of turbulence). With a sensitivity study on resolution, ranging the (horizontal) grid spacing from 3.125 to 100 m in factors of two, we

addressed the role of the fraction of resolved turbulence on the development of the NBL, and implication of NBL biases on the consecutive day of dry convection. The roles of moisture and radiation were excluded from the experiments; if a relatively simple dry case is poorly represented, then more complex cases involving moist convection will surely be influenced.

From the results of our numerical experiments, we can draw a number of conclusions. As expected, the rate of resolved turbulence in the NBL quickly decreases with increasing grid spacing. At grid spacings as coarse as 100 m, no NBL turbulence is resolved and the NBL development is predominantly driven by the SGS model. Under these conditions, the NBL is poorly represented with relative biases in the NBL depth of 100%–120%, and absolute biases in the bulk NBL temperature of 2–3 K. These biases are the result of both the SGS model, causing excessive vertical mixing at low resolutions, and feedbacks between the LSM and the atmosphere. The latter allows for a more realistic response of surface processes to (biases in) the atmosphere, relaxing the strict coupling that would be introduced with the use of a prescribed surface temperature or flux. Despite the large biases in the NBL, the influence on the consecutive day of convection is limited: maximum biases in the afternoon mixed-layer depth and temperature are approximately 100 m and 0.5 K, respectively. As these biases are positively correlated—an underestimation of the NBL depth corresponds to an underestimation of the ABL temperature—the biases compete and partially compensate their individual influence on the mixed-layer top relative humidity, resulting in maximum differences of 0% to -3%. This insensitivity of the relative humidity is important for correctly timing the onset of moist convection, as a precursor for deeper moist convection and precipitation. The authors remind the reader that our simulations excluded moisture and therefore only provide a first-order estimate, neglecting the influence of potential biases in the moisture mixing ratio.

For applications focused on daytime convection, in which biases during the NBL period are tolerable, these findings are promising. The use of relatively coarse resolutions greatly decreases the required computational resources, opening the opportunity for employing LES to study the diurnal cycle of convection at mesoalpha scales (20–2000 km). However, our study only addressed the dynamical aspects in the absence of moisture and radiation. Whether moisture (fog) and radiation can, in particular cases, further amplify the NBL biases and/or daytime convection is currently unknown. Also, our study predominantly focused on the mean thermodynamic structure of the ABL. A more detailed analysis of the influence of grid spacing on (shallow) convection, similar to *Sullivan and Patton* [2011] and extending the work of *Bryan et al*. [2003] would be interesting. Both topics will need to be addressed in the future research.

Appendix A : Sampling Criteria Measurement Data

We sample clear nights based on the difference in incoming longwave radiation (LW_{in}) between measurements and a theoretical value calculated using the 2 m temperature ($T_{2\text{m}}$) and Stefan-Boltzmann's law. In the presence (absence) of clouds, the difference $\delta Q = \sigma T_{2\text{m}}^4 - LW_{\text{in}}$ (with $\sigma = 5.67 \times 10^8 \text{Wm}^{-2}\text{K}^{-4}$) is expected to be small (large). The threshold for this difference, and the missampling that it introduces, was studied using cloud cover observations from CESAR as shown in Figure A1. For samples with a large observed cloud cover, δQ is typically less than 50 W m^{-2}, while for clear nights the majority of the samples have δQ larger than 50 W m^{-2}. Using a threshold $\delta Q \geq 50 \text{Wm}^{-2}$ to subsample the clear nights, and defining a cloud cover of $\geq 30\%$ as cloudy, results in a missampling of 11% (dashed area).

Appendix B : Description Land-Surface Model

The parameterization of the land-surface model (LSM) is inspired by the ECMWF IFS documentation [*ECMWF*, 2011]. Equation or section numbers prepended with "IFS" refer to the latter document. In the absence of moisture, the surface energy balance (SEB) is defined as:

$$Q_{\text{net}} = LW_{\text{in}} - LW_{\text{out}} + SW_{\text{in}} - SW_{\text{out}} = H + G, \tag{B1}$$

with Q_{net} the net surface radiation, LW and SW the longwave and shortwave, incoming (in) and outgoing (out) radiative fluxes, and H and G the surface sensible and soil heat flux. The different radiative components are prescribed or parameterized. The longwave components are defined as $LW_{\text{in}} = 300 \text{Wm}^{-2}$ and $LW_{\text{out}} = \sigma T_s^4$, with T_s the surface (skin) temperature. Shortwave radiation is parameterized using the geographical location, time and day of year [*Stull*, 1988, pp. 255–258] using 48°N, Julian date 196 starting at 1500 UTC), and a prescribed surface albedo. With the latent heat flux excluded from the SEB (equation (B1)),

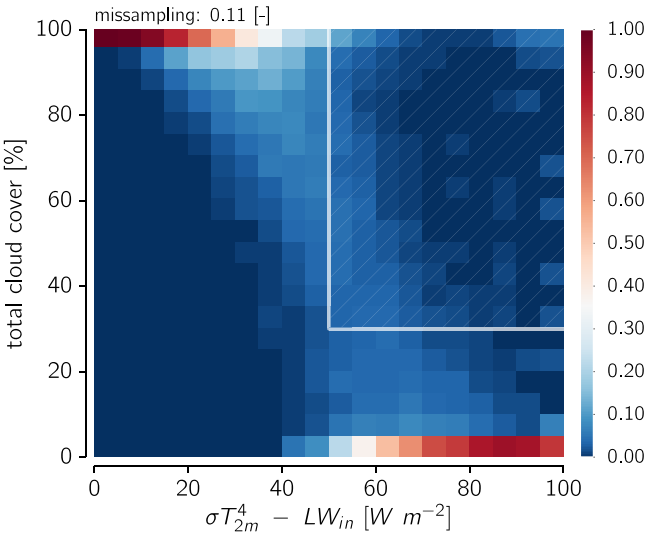

Figure A1. Two-dimensional histogram of the measured cloud fraction versus $\delta Q = \sigma T_{2m}^4 - LW_{in}$. For each vertical bin, the probability is normalized, i.e., each column has a total probability of 1. The hashed square indicates the missampling (see text).

the surface albedo was increased to 0.65 to prevent unrealistic daytime sensible heat fluxes. The resulting heat flux, as shown in Figure 3, is representative for both the Cabauw and Hamburg site. With the surface fluxes defined as:

$$H = \frac{\rho c_p}{r_a}(\theta_s - \theta_a), \tag{B2}$$

$$G = \Lambda_{sk}(T_s - T_{soil}), \tag{B3}$$

with ρ the (surface) air density, c_p the specific heat capacity of air at constant pressure (1005 J kg^{-1} K^{-1}), r_a the aerodynamic resistance, θ_a the potential temperature at the lowest model level, T_s (θ_s) the surface (potential) temperature, Λ_{sk} the thermal conductivity of the skin layer, and T_{soil} the temperature of the top soil layer. The aerodynamic resistance is defined as $1/r_a = C_H|U|$, with $|U|$ the absolute wind speed at the lowest model level, and C_H the transfer coefficient of heat (equation (IFS-3.15)). The latter is calculated using the integrated stability functions as defined in equations (IFS-3.20) and (IFS-3.22), calculating the Obukhov length as defined in section IFS-3.2.3.

Assuming that the heat capacity of the skin layer is zero, the surface temperature can explicitly be solved from equations (B1)–(B3). Four soil layers are used with their midpoints at {0.035, 0.175, 0.64, and 1.5} m depth, with initial temperatures (gradient typical for the study area at hand) of {291.0, 290.7, 289.8, 287.9} degrees, respectively. Evolution of the soil temperature follows a diffusion equation (equation (IFS-8.54)):

$$(\rho C)_{soil}\frac{\partial T_{soil}}{\partial t} = \lambda_T \frac{\partial^2 T_{soil}}{\partial z^2}, \tag{B4}$$

with $(\rho C)_{soil} = 2.19 \times 10^6$ J m^{-3} K^{-1} and λ_T a prescribed thermal conductivity of 1.255 W m^{-1} K^{-1}. The latter value is representative for a loamy soil at a volumetric soil moisture content of 0.247 m^3 m^{-3}.

Acknowledgments

This work was funded by the Federal Ministry of Education and Research in Germany (BMBF) through the research program *High-Definition Clouds and Precipitation for Climate Prediction*—HD(CP)2 (FKZ: 01LK1202E). Computing resources were provided by the German Climate Computing Center (DKRZ), Hamburg. The authors thank the University of Hamburg and the Cabauw Experimental Site for Atmospheric Research (CESAR) for providing the measurement data and Rieke Heinze for detailed comments on a draft of this manuscript. The UCLA-LES source code is available at http://gitorious.org/uclales/. Data used for this study are archived at the German Climate Computing Center (DKRZ). Both the data, and input files necessary to reproduce the experiments with UCLA-LES, are available from the authors upon request (bart.vanstratum@mpimet.mpg.de).

References

Baldauf, M., A. Seifert, J. Frstner, D. Majewski, M. Raschendorfer, and T. Reinhardt (2011), Operational convective-scale numerical weather prediction with the cosmo model: Description and sensitivities, *Mon. Weather Rev.*, *139*(12), 3887–3905.

Basu, S., J.-F. Vinuesa, and A. Swift (2008a), Dynamic LES modeling of a diurnal cycle, *J. Appl. Meteorol. Climatol.*, *47*(4), 1156–1174.

Basu, S., A. A. Holtslag, B. J. Wiel, A. F. Moene, and G.-J. Steeneveld (2008b), An inconvenient truth about using sensible heat flux as a surface boundary condition in models under stably stratified regimes, *Acta Geophys.*, *56*(1), 88–99, doi:10.2478/s11600-007-0038-y.

Beare, R. J., et al. (2006), An intercomparison of large-eddy simulations of the stable boundary layer, *Boundary Layer Meteorol.*, *118*(2), 247–272.

Bou-Zeid, E., C. Meneveau, and M. Parlange (2005), A scale-dependent Lagrangian dynamic model for large eddy simulation of complex turbulent flows, *Phys. Fluids*, *17*(2), 1–18.

Brown, A. R., et al. (2002), Large-eddy simulation of the diurnal cycle of shallow cumulus convection over land, *Q. J. R. Meteorol. Soc.*, *128*, 1075–1093.

Brümmer, B., I. Lange, and H. Konow (2012), Atmospheric boundary layer measurements at the 280 m high Hamburg weather mast 1995–2011: Mean annual and diurnal cycles, *Meteorol. Z.*, *21*(4), 319–335.

Bryan, G. H., J. C. Wyngaard, and J. M. Fritsch (2003), Resolution requirements for the simulation of deep moist convection, *Mon. Weather Rev.*, *131*, 2394–2416.

Chung, D., and G. Matheou (2014), Large-eddy simulation of stratified turbulence. Part I: A vortex-based subgrid-scale model, *J. Atmos. Sci.*, *71*, 1863–1879, doi:10.1175/jas-d-13-0126.1.

de Roode, S. R., F. C. Bosveld, and P. S. Kroon (2010), Dew formation, eddy-correlation latent heat fluxes, and the surface energy imbalance at Cabauw during stable conditions, *Boundary Layer Meteorol.*, *135*(3), 369–383, doi:10.1007/s10546-010-9476-1.

Duynkerke, P. G. (1999), Turbulence, radiation and fog in Dutch stable boundary layers, *Boundary Layer Meteorol.*, *90*(3), 447–477, doi:10.1023/A:1026441904734.

ECMWF (2011), IFS documentation Cy37r2—Part IV: Physical processes, *Tech. Rep. Cy37r2*, European Centre for Medium-Range Weather Forecasts, Reading, U. K.

Fernando, H. J. S., and J. C. Weil (2010), Whither the stable boundary layer?, *Bull. Am. Meteorol. Soc.*, *91*(11), 1475–1484.
Garratt, J. R., and R. A. Brost (1981), Radiative cooling effects within and above the nocturnal boundary layer, *J. Atmos. Sci.*, *38*(12), 2730–2746.
Holloway, C. E., S. J. Woolnough, and G. M. S. Lister (2012), Precipitation distributions for explicit versus parameterized convection in a large domain high resolution tropical case study, *Q. J. R. Meteorol. Soc.*, *138*(668), 1692–1708, doi:10.1002/qj.1903.
Holtslag, A. A. M., G. J. Steeneveld, and B. J. H. Wiel (2007), Role of land-surface temperature feedback on model performance for the stable boundary layer, in *Atmospheric Boundary Layers*, edited by A. Baklanov and B. Grisogono, pp. 205–220, Springer, N. Y.
Holtslag, A. A. M., et al. (2013), Stable atmospheric boundary layers and diurnal cycles: Challenges for weather and climate models, *Bull. Am. Meteorol. Soc.*, *94*(11), 1691–1706.
Honnert, R., V. Masson, and F. Couvreux (2011), A diagnostic for evaluating the representation of turbulence in atmospheric models at the kilometric scale, *J. Atmos. Sci.*, *68*, 3112–3131.
Huang, H.-Y., B. Stevens, and S. Margulis (2008), Application of dynamic subgrid-scale models for large-eddy simulation of the daytime convective boundary layer over heterogeneous surfaces, *Boundary Layer Meteorol.*, *126*(3), 327–348.
Jakob, C. (2010), Accelerating progress in global atmospheric model development through improved parameterizations: Challenges, opportunities, and strategies, *Bull. Am. Meteorol. Soc.*, *91*(7), 869–875.
Kleissl, J., V. Kumar, C. Meneveau, and M. B. Parlange (2006), Numerical study of dynamic smagorinsky models in large-eddy simulation of the atmospheric boundary layer: Validation in stable and unstable conditions, *Water Resour. Res.*, *42*, W06D10, doi:10.1029/2005WR004685.
Kosovic, B., and J. A. Curry (2000), A large eddy simulation study of a quasi-steady, stably stratified atmospheric boundary layer, *J. Atmos. Sci.*, *57*(8), 1052–1068.
Kumar, V., J. Kleissl, C. Meneveau, and M. Parlange (2006), Large-eddy simulation of a diurnal cycle of the atmospheric boundary layer: Atmospheric stability and scaling issues, *Water Resour. Res.*, *42*, W06D09, doi:10.1029/2005WR004651.
Kumar, V., G. Svensson, A. A. M. Holtslag, C. Meneveau, and M. B. Parlange (2010), Impact of surface flux formulations and geostrophic forcing on large-eddy simulations of diurnal atmospheric boundary layer flow, *J. Appl. Meteorol. Climatol.*, *49*(7), 1496–1516.
Lévêque, E., F. Toschi, L. Shao, and J.-P. Bertoglio (2007), Shear-improved smagorinsky model for large-eddy simulation of wall-bounded turbulent flows, *J. Fluid Mech.*, *570*, 491–502.
Lilly, D. K. (1962), On the numerical simulation of buoyant convection, *Tellus*, *14*(2), 148–172, doi:10.1111/j.2153-3490.1962.tb00128.x.
Lilly, D. K. (1966), The representation of small-scale turbulence in numerical simulation experiments, *Tech. Rep. 281*, Nat. Cent. for Atmos. Res., Boulder, Colo.
Mason, P. J., and S. H. Derbyshire (1990), Large-eddy simulation of the stably-stratified atmospheric boundary layer, *Boundary Layer Meteorol.*, *53*(1–2), 117–162, doi:10.1007/BF00122467.
Mason, P. J., and D. J. Thomson (1992), Stochastic backscatter in large-eddy simulations of boundary layers, *J. Fluid Mech.*, *242*, 51–78.
Miyamoto, Y., Y. Kajikawa, R. Yoshida, T. Yamaura, H. Yashiro, and H. Tomita (2013), Deep moist atmospheric convection in a subkilometer global simulation, *Geophys. Res. Lett.*, *40*, 4922–4926, doi:10.1002/grl.50944.
Ogura, Y., and N. A. Phillips (1962), Scale analysis of deep and shallow convection in the atmosphere, *J. Atmos. Sci.*, *19*(2), 173–179.
Pino, D., J. Vilà-Guerau de Arellano, and P. G. Duynkerke (2003), The contribution of shear to the evolution of a convective boundary layer, *J. Atmos. Sci.*, *60*(16), 1913–1926.
Pope, S. (2000), *Turbulent Flows*, Cambridge Univ. Press, Cambridge, U. K.
Richardson, H., S. Basu, and A. Holtslag (2013), Improving stable boundary-layer height estimation using a stability-dependent critical bulk Richardson number, *Boundary Layer Meteorol.*, *148*(1), 93–109.
Smagorinsky, J. (1963), General circulation experiments with the primitive equations, *Mon. Weather Rev.*, *91*(3), 99–164.
Stevens, B., and S. Bony (2013), What are climate models missing?, *Science*, *340*(6136), 1053–1054.
Stevens, B., et al. (2005), Evaluation of large-eddy simulations via observations of nocturnal marine stratocumulus, *Mon. Weather Rev.*, *133*(6), 1443–1462.
Stull, R. B. (1988), *An Introduction to Boundary Layer Meteorology*, Kluwer Acad. Publ., Dordrecht, Netherlands.
Sullivan, P. P., and E. G. Patton (2011), The effect of mesh resolution on convective boundary layer statistics and structures generated by large-eddy simulation, *J. Atmos. Sci.*, *68*(10), 2395–2415.
van Stratum, B. J. H., J. Vilà-Guerau de Arellano, C. C. van Heerwaarden, and H. G. Ouwersloot (2014), Subcloud-layer feedbacks driven by the mass flux of shallow cumulus convection over land, *J. Atmos. Sci.*, *71*(3), 881–895.
Van Ulden, A. P., and J. Wieringa (1996), Atmospheric boundary layer research at Cabauw, *Boundary Layer Meteorol.*, *78*(1–2), 39–69.
Vilà-Guerau de Arellano, J. (2007), Role of nocturnal turbulence and advection in the formation of shallow cumulus over land, *Q. J. R. Meteorol. Soc.*, *133*(628), 1615–1627.
Wicker, L. J., and W. C. Skamarock (2002), Time-splitting methods for elastic models using forward time schemes, *Mon. Weather Rev.*, *130*(8), 2088–2097.
Wyngaard, J. C. (2004), Toward numerical modeling in the "Terra Incognita", *J. Atmos. Sci.*, *3*(2), 1816–1826.
Zhou, B., J. S. Simon, and F. K. Chow (2014), The convective boundary layer in the Terra Incognita, *J. Atmos. Sci.*, *71*(7), 2545–2563.